Large eddy simulations of a circular cylinder at Reynolds numbers surrounding the drag crisis

Thomas P. Lloyd[a,b,*], Marion James[b]

[a] *MARIN Academy, Maritime Research Institute Netherlands, Wageningen, The Netherlands;*
[b] *Fluid Structure Interactions Research Group, University of Southampton, Southampton, United Kingdom;*

Abstract

Large eddy simulations of the flow around a circular cylinder at high Reynolds numbers are reported. Five Reynolds numbers were chosen, such that the *drag crisis* was captured. A total of 18 cases were computed to investigate the effect of gridding strategy, domain width, turbulence modelling and numerical schemes on the results. It was found that unstructured grids provide better resolution of key flow features, when a 'reasonable' grid size is to be maintained.

When using coarse grids for large eddy simuation, the effect of the turbulence models and numerical schemes becomes more pronounced. The dynamic mixed Smagorinsky model was found to be superior to the Smagorinsky model, since the model coefficient is allowed to dynamically adjust based on the local flow and grid size. A blended upwind-central convection scheme was also found to provide the best accuracy, since a fully central scheme exhibits artificial wiggles which pollute the entire solution.

Mean drag, fluctuating lift and Strouhal number are compared to experiments and empirical estimates for Reynolds numbers ranging from $6.31 \times 10^4 - 5.06 \times 10^5$. In terms of the drag coefficient, the drag crisis is well captured by the present simulations, although the other integral quantities (*rms* lift and Strouhal number) less so. For the lowest Reynolds number, the drag is seen to be most sensitive to the domain width, while at the higher Reynolds numbers the grid resolution plays a more important role.

Keywords: circular cylinder, drag crisis, high Reynolds number, large eddy simulation

1. Introduction

The flow around circular cylinders is of considerable interest within the areas of turbulence research and engineering analysis. Predicting cylinder forces is particularly important when aiming to reduce vortex-induced vibration (VIV), which may occur in a maritime context *e.g.* risers. Such fluid-structure interaction scenarios have been investigated both experimentally [1] and computationally [2]. However, accurate prediction of the unsteady forces on smooth fixed circular cylinders still remains a challenge for computational methods typically used in engineering.

Cylinder flows have received a considerable amount of research attention due to the complex flow behaviour behind the cylinder, which is highly Reynolds number dependent. Reviews of the vortex-shedding behaviour of circular cylinders are provided by Williamson [3] and Norberg [4]. For Reynolds numbers ($Re = U_0 D/\nu$) relevant in maritime engineering, the flow exhibits two regimes, nominally separated at $\sim 2 \times 10^5$ (see [3]). For:

- $Re < 2\times10^5$, the wake is turbulent while the attached flow is laminar; the shear layer transitions to turbulence via Kelvin-Helmholtz instability modes, with the length of the shear layer reducing as the Reynolds number increases.
- $Re > 2\times10^5$, transition occurs on the cylinder surface (boundary layer becomes turbulent); the flow therefore remains attached for longer, resulting in a large reduction in drag.

It is this drag reduction, known as the *drag crisis*, which is of particular interest in engineering, as large fluctuating loads have implications for structural design and material fatigue life.

Computational studies of circular cylinders have utilise a number of turbulence modelling techniques. Rosetti *et al.*[5] presented a detailed verification and validation study using the unsteady Reynolds-averaged Navier-Stokes (URANS) equations for a wide range of Reynolds numbers. For two-dimensional computations, these authors found that the drag crisis was not well captured using this approach, which models all the scales of turbulence. Vaz *et al.* [6] compared detached eddy simulation (DES) to URANS, but found it did not consistently provided superior predictive capabilities over some RANS models. Very high Reynolds numbers (10^6) were treated using DES in [7], yet the authors note limited success as Reynolds number increases, due to coarse grids and simplified transition modelling. Since DES typically exhibits a

*Corresponding author
Email address: T.P.Lloyd@soton.ac.uk (Thomas P. Lloyd)

RANS-like behaviour in the boundary layer, the inaccuracies associated with the RANS turbulence model remain. Large eddy simulations, in which only the small turbulence scales are modelled, have typically focussed on low Reynolds numbers where the grid resolution requirements are less demanding. There is, for example, a large body of literature concerning $Re = 3900$ *e.g.* see [8, 9, 10, 11, 12]. Whilst good agreement between numerical and experimental data is typically seen, grid sizes may still be regarded as large (*e.g.* 6×10^6 grid cells [9]). At higher Reynolds numbers, much larger grids have been used. For example, at $Re = 1.4 \times 10^5$, grids contain up to 90 million unstructured cells [13, 14], which are clearly prohibitive for most engineering applications where computational power is limited. Breuer [15] presented large eddy simulations at $Re = 1.4 \times 10^5$, investigating the effects of grid resolution, domain size and subgrid turbulence model. The maximum grid size used was 6.76 million cells. While the effects of subgrid turbulence model and grid density are difficult to separate in large eddy simulation (LES), this study showed significant sensitivity of the integral results to the choice of subgrid model.

In this paper we analyse the performance of LES for high Reynolds number cylinder flows, suitable for 'engineering' applications. The aim was to understand the impact of key modelling decisions on the accuracy of predictions, while maintaining 'reasonable' grid sizes. §2 outlines the chosen test case and set-up of the computational domain. In §3, an overview of the computational methods used is provided. Results are presented in three sections: §4 details the effects of grid refinement for both structured and unstructured grids for a single Reynolds number; §5 analyses the chosen numerical schemes at the same Re; and §6 reports the results for five Reynolds numbers from 6.31×10^4 to 5.06×10^5. Finally, discussions and conclusions are made in §7.

2. Test Case

The test case was designed to replicate the experiments of Wilde *et al.*[1], with a cylinder diameter (D) of 0.2 m. Although a span (S) of 3.4 m was tested, simulations are limited to $0.1S$. The domain is represented in Figure 1, showing the coordinate system, domain size and boundary designations. The z direction is along the cylinder span. The domain size and boundary conditions are similar to those from other CFD investigations of cylinders *e.g.* see [5, 15].

A fixed value Dirichlet velocity inlet is used, with Neumann pressure. The outlet used a convective condition, which allows vortices to exit the domain without reflection, while a symmetry condition was prescribed at the top and bottom boundaries. A no-slip condition was applied to the cylinder, with periodic boundaries used at the sides in order to approximate an infinite span.

For all the cases presented, the flow is initialised from a previous turbulent solution, and allowed to develop for 20 shedding cycles. After this statistics are recorded for a further 20 cycles.

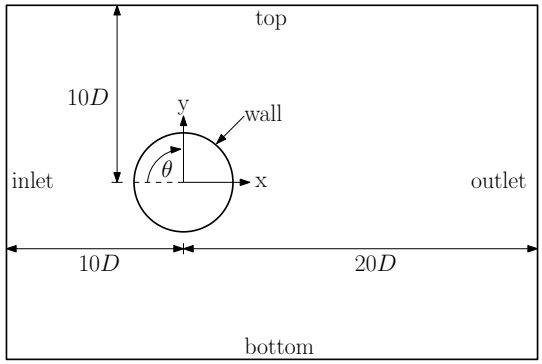

Figure 1: Schematic of circular cylinder test case domain.

3. Modelling Approach

All simulations were conducted using the OpenFOAM® 2.2.0 libraries. The code consists of dynamically linked C++ files for pre- and post-processing, as well as solution, using the finite volume method. Further details of the code may be found in [16, 17]. In the finite volume method, the governing equations are discretised into volumes (cells), permitting arbitrary cell shapes suitable for gridding complex geometries. The field variables are colocated at the cell centres. In order to avoid unphysical staggering of the solution, a 'Rhie-Chow'-type [18] correction is applied with the pressure implicit splitting of operators (PISO) algorithm [19]. All discretisation schemes used are second-order, apart from convective acceleration; investigation of different convection schemes is presented in Section 5. Linear solution is achieved using the biconjugate gradient method for velocity, and general algebraic multigrid method for pressure. The linear solver was set to exit the iteration loop upon reaching a final residual value of 10^{-6} for pressure and 10^{-9} for all other variables.

3.1. Turbulence modelling

Large eddy simulation has been used throughout this study. LES lies between direct numerical simulation (DNS) and URANS methods in terms of flow resolution. The filtered governing equations are solved, meaning the large scale turbulence is resolved on the grid, while scales smaller than the grid are modelled. These may be written as

$$\nabla \cdot \overline{\boldsymbol{u}} = 0 \tag{1a}$$

and

$$\partial_t(\overline{\boldsymbol{u}}) + \nabla \cdot (\overline{\boldsymbol{u}} \otimes \overline{\boldsymbol{u}}) = -\frac{1}{\rho}\nabla p + \nu_{eff}\nabla^2\overline{\boldsymbol{u}}, \tag{1b}$$

where overbars here denote a filtered (not a mean) quantity, $\boldsymbol{u}$ is the velocity vector, ρ the fluid density, p the

pressure and $\nu_{eff} = \nu + \nu_{sgs}$ the effective viscosity, consisting of the molecular viscosity ν and the subgrid scale viscosity ν_{sgs}. In an ideal LES, 80% of the total turbulence kinetic energy should be resolved [20]. See [21] for a detailed background on LES. Wall-resolved LES grids require $(\Delta x^+, y_w^+, \Delta z^+) = (50 - 150, 1, 15 - 40)$ according to [22]. Although these criteria are less onerous than DNS, a total grid cell scaling of $N_{xyz} \propto Re^{1.8}$ means that achieving a well resolved LES grid at high Reynolds number may not always be possible. In this case, the *subgrid* turbulence model used may have a larger impact on the results. Furthermore, estimating the required grid size for complex flows may not be possible *a priori*.

In this paper, we compare two subgrid models. These are designed to account for the interactions between the modelled scales and the resolved flow field. Here, a brief outline of popular models is provided; Sagaut [21] describes the derivation of numerous subgrid models in more detail. The simplest subgrid model is that first derived by Smagorinsky [23]. Utilising the Boussinesq hypothesis, the subgrid stress tensor is modelled as proportional to the resolved strain field, which may be written as

$$\tau^S - \frac{1}{3}\tau^S \cdot \boldsymbol{I} = -\nu_{sgs}\overline{\boldsymbol{S}}. \tag{2}$$

The subgrid viscosity (equivalent to the turbulence viscosity in RANS) takes the form

$$\nu_{sgs} = \left(C_S\overline{\Delta}\right)^2|\overline{\boldsymbol{S}}| \tag{3}$$

with $|\boldsymbol{S}| = (2\boldsymbol{S}\cdot\boldsymbol{S})^{1/2}$ and $\overline{\Delta}$ the grid cutoff size. The Smagorinsky constant C_S takes a value of *0.1 - 0.2*, depending on the flow type. An alternative approach to functional modelling is the *structural* model class, which includes those based on the *scale similarity* hypothesis. This states that the largest subgrid scales are analogous to the smallest resolved scales, thus better representing the structure of the subgrid stress tensor. This class of models better accounts for the effect of the subgrid scales on the resolved field. The subgrid tensor for the Bardina model [24] is obtained by applying a double filtering operation:

$$\tau^B = \overline{\boldsymbol{u}\otimes\boldsymbol{u}} - \overline{\boldsymbol{u}}\otimes\overline{\boldsymbol{u}} \approx \overline{\overline{\boldsymbol{u}}\otimes\overline{\boldsymbol{u}}} - \overline{\overline{\boldsymbol{u}}}\otimes\overline{\overline{\boldsymbol{u}}}. \tag{4}$$

Since the coefficient C_S is dependent on the grid resolution as well as the flow type, improvements to the subgrid model can be made be dynamically evaluating C_S, both spatially and temporally. Germano *et al.* [25] used a *test filter* (denoted by a *caret*) to define the *resolved stress tensor* $\boldsymbol{L} = \widehat{\overline{\boldsymbol{u}}\otimes\overline{\boldsymbol{u}}} - \hat{\overline{\boldsymbol{u}}}\otimes\hat{\overline{\boldsymbol{u}}}$. The resolved stress tensor represents scales between the test and grid filter cutoff. The test filter uses a different filter width (typically $\hat{\Delta} = 2\overline{\Delta}$). Lilly [26] showed that the Smagorinsky constant may be written as

$$C_S^2 = \left(\frac{\boldsymbol{L}\cdot\boldsymbol{M}}{\boldsymbol{M}\cdot\boldsymbol{M}}\right), \tag{5}$$

where $\boldsymbol{M} = 2(\overline{\Delta}/\hat{\Delta})^2|\hat{\overline{\boldsymbol{S}}}|\hat{\overline{\boldsymbol{S}}} - \hat{\Delta}^2\widehat{|\overline{\boldsymbol{S}}|\overline{\boldsymbol{S}}}$.

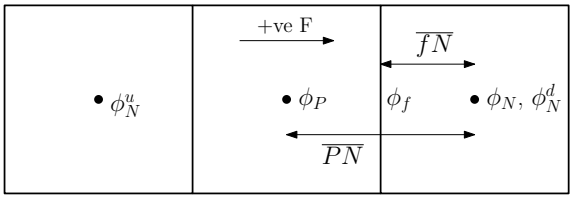

Figure 2: Definitions for interpolation of face values by convection differencing schemes.

To overcome the disadvantages of both structural and functional (such as Smagorinsky) models, *mixed* models have been proposed. These aim to combine to better energy transfer and vorticity production of functional models with the subgrid stress tensor structure of the structural (scale similarity) models. The dynamic mixed Smagorinsky model [27] can be written in the form

$$\tau^S - \frac{1}{3}\tau^S\cdot\boldsymbol{I} = \frac{1}{2}(-2\nu_{sgs}\overline{\boldsymbol{S}} + \tau^B - \frac{1}{3}\tau^B\boldsymbol{I}). \tag{6}$$

The dynamic Smagorinsky constant is now

$$C_S^2 = \frac{1}{2}\left(\frac{(\boldsymbol{L}-\boldsymbol{B})\cdot\boldsymbol{M}}{\boldsymbol{M}\cdot\boldsymbol{M}}\right) \tag{7}$$

where $\boldsymbol{B} = \widehat{\overline{\overline{\boldsymbol{u}}\otimes\overline{\boldsymbol{u}}}} - \hat{\overline{\overline{\boldsymbol{u}}}}\otimes\hat{\overline{\overline{\boldsymbol{u}}}}$. See [9, 28, 29] for evaluations of subgrid models implemented into OpenFOAM. In this paper, we compare the simplest (Smagorinsky, denoted S) and most sophisticated (dynamic mixed Smagorinsky, denoted DMS) of these models.

3.2. Numerical schemes

We also present investigations of convection differencing schemes. The focus is on the effect of introducing upwinding to central schemes. Typically, central schemes are preferred for LES within the finite-volume method, where the time-dependent spatial character of the flow field should be resolved. However, some upwinding may sometimes be necessary in order to maintain stability and avoid artificial wiggles in the solution, particularly on under-resolved grids.

The central scheme is referred to here as a *linear* scheme, since it is based on linear interpolation of the face values from the adjacent cell centre values. The scheme therefore possesses second-order accuracy. The face value (subscript 'f') of a variable ϕ is then

$$\phi_f = d_f\phi_P + (1-d_f)\phi_N, \tag{8}$$

with 'P' and 'N' the cell centre values of two neighbouring cells, and $d_f = \overline{fN}/\overline{PN}$. On coarse grids however, the central scheme may not possess boundedness and stability, due to the Péclet number (ratio of convection to diffusion) exceeding two [30]. Stability may be intriduced using an upwind scheme, but typically at the expense of accuracy. An upwind scheme is first-order, and takes the face value

Table 1: Descriptions of convection schemes investigated.

Scheme	Type	Description
linear	central	second-order
filteredLinear	central/upwind	first/second-order; upwinding added using dynamic Sweby limiter
limitedLinear	central/upwind	first/second-order; upwinding added using fixed value for Sweby limiter
QUICK	upwind	second-order (on unstructured grids); fixed amount of upwinding

as equal to the cell centre value in the upwind direction *i.e.*

$$\phi_f = \begin{cases} \phi_P & \text{if } F \geq 0 \\ \phi_N & \text{if } F \leq 0. \end{cases} \tag{9}$$

where F is the flux direction. The upwind direction is determined by the direction of the flux through the cell. Since upwind schemes are too diffusive for LES, we tested the performance of several blended upwind-central schemes within *OpenFOAM*. The amount of upwinding introduced is controlled by the parameter Ψ, referred to as the Sweby limiter [31]. A face flux is calculated as

$$\phi_f = \phi_f^c + \Psi\left(\phi_f^u - \phi_f^c\right), \tag{10}$$

where the superscript 'c' and 'u' refer to the central and upwind schemes. Based on Equation 10, $\Psi = 1$ corresponds to fully upwind and $\Psi = 0$ to fully central. Descriptions of the specific schemes investigated are provided in Table 1, while further details may be found in [29].

Another scheme which combines upwinding with higher-order accuracy is *QUICK* [32]. Using a three-point stencil, the face value is

$$\phi_f = \frac{3}{8}\phi_N^d + \frac{3}{4}\phi_P + \frac{1}{8}\phi_N^u. \tag{11}$$

The superscript 'd' denotes the downwind value.

Time stepping should also be second-order in finite volume LES. Here, we used an implicit backward differencing scheme (referred to as BDF2), which is unconditionally stable. The time step is therefore not dictated by the time scheme but by the pressure-velocity coupling method (solution algorithm). The stability of the solution algorithm can be related to the Courant number $CFL = |u\Delta t|/\Delta x$. As a simple example, an eddy with convection speed u will travel more than one cell length Δx if $CFL > 1$. This will clearly affect the accuracy of the resolved turbulence. One commonly used algorithm is the PISO method [19], which requires $CFL < 1$ for stability. It should be noted that the mean CFL is much lower, typically ~ 0.02.

4. Grid Sensitivity Study

In this first results section, only a single Reynolds number is addressed. At $Re = 1.26 \times 10^5$, we expect features including laminar boundary layers, Kelvin-Helmholtz instabilities and a turbulent wake. Hence this is a challenging flow to simulate, and provides a good test case for grid sensitivity and influence of numerical setup.

Two meshing approaches were adopted: structured and unstructured. Structured grids are often regarded as possessing higher quality cells and therefore providing faster solution convergence and more accurate results. However, the fine wall grid required for LES means the structured approach typically requires more cells than an unstructured grid. Hence, grid resolution (particularly in the spanwise direction) may be reduced in order to maintain a feasible cell count. In the unstructured approach, refinement may be targeted at certain regions whilst maintaining reasonable grid sizes. This approach has also been adopted by [11]. Convergence and accuracy may be sacrificed however.

For this study, we used the commercial software *Pointwise V17.0®* to generate structured grids, and the OpenFOAM utility *snappyHexMesh* for unstructured grids. Table 2 details the total size and estimated wall resolution of the grids used. Comparing to the criterion outlined in Section 3.1, the resolution in the $x-$ and $y-$ directions is reasonable, while the z-direction is coarse. Note however that the cell size in the wake region increases relatively quickly due to the grid stretching (in the structured case) or hanging node refinement technique (unstructured).

For both gridding techniques, grid sizes of approximately two, four and six million cells were targeted. In the structured case, the additional cells come purely from spanwise grid refinement; the unstructured grids use a global grid refinement ratio of ~ 1.15, while the boundary layer grid remains unchanged in terms of wall-normal growth. This results in $y_w^+ \approx 0.5$ for all grids. Differences in the approaches are evident in Figure 3.

Since the grids were not systematically refined, that is, every cell scaled equally in all directions, the results presented do not constitute a rigorous grid refinement study. However the effects of spanwise grid refinement (particularly important for high Reynolds number LES) and grid density in the cylinder wake are still evident in the results.

Table 2: Summary of grid sizes and estimated wall resolution used in sensitivity study. Wall units refer to $Re = 1.26 \times 10^5$ case.

Name	Size / 10^6	Δx_w^+	y_w^+	Δz_w^+
S1	2.0	110	0.5	170
S2	4.5	110	0.5	75
S3	6.0	110	0.5	57
U1	2.0	140	0.5	140
U2	4.0	110	0.5	110
U3	5.6	95	0.5	95

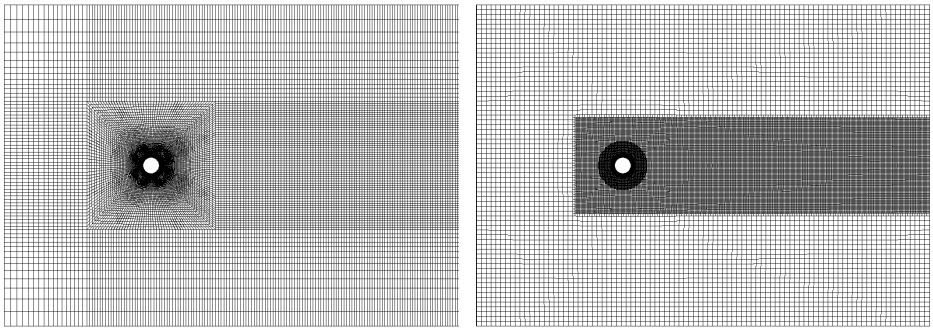

(a) structured grid overview

(b) unstructured grid overview

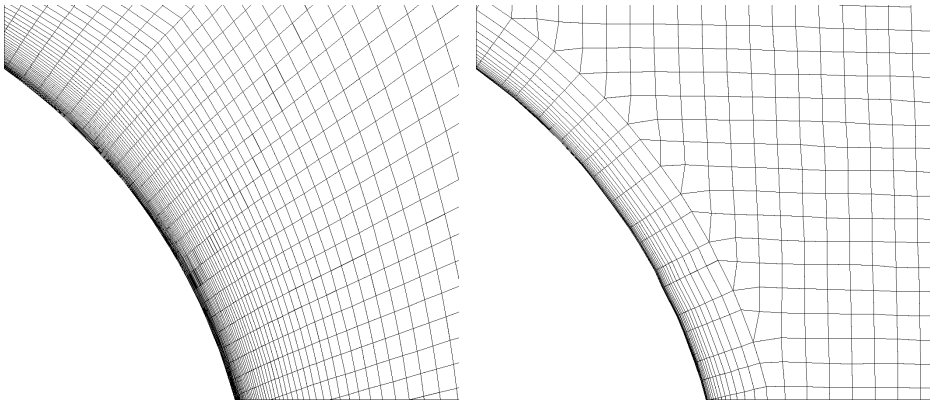

(c) structured grid close up

(d) unstructured grid close up

Figure 3: Views of the structured and unstructured grids (in order to aid visualisation, coarsest grids shown)

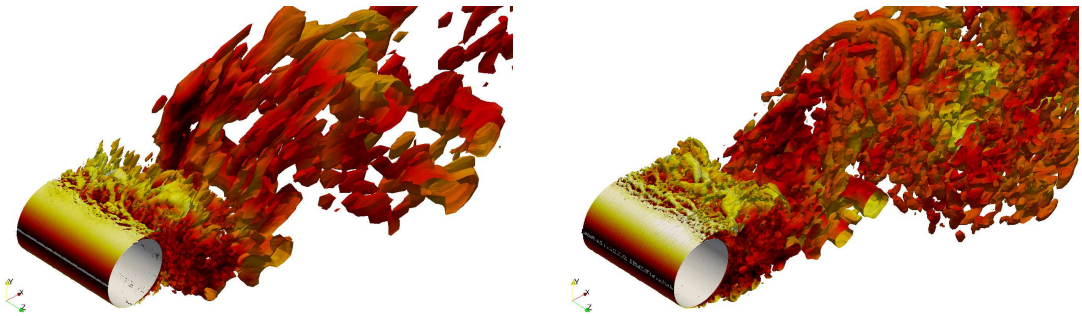

(a) S1 (Case 4B)

(b) U1 (Case 4E)

Figure 4: Isosurfaces of $Q = 10\ s^{-1}$, coloured by streamwise velocity. $Re = 1.26 \times 10^5$.

Figure 4 shows visualisations of vortical structures in terms of Q, the second invariant of the velocity gradient tensor. Positive values of Q show turbulence structures undergoing rotation. Here the wake coarsening of the structured grid dramatically reduces the resolution of fine scale turbulence, which are better captured on the unstructured grid. The square cells close to the cylinder also appear to improve the capture of the shear layer.

A summary of integral parameters for all cases (results from Sections 4-6) is given in Table 3. We do not present quantitative grid refinement assessment *i.e. verification*, since as the grid is refined the contribution of the subgrid model changes. Thus grid and modelling errors cannot be fully separated. For this Reynolds number, typical experimental and empirical values of integral parameters are: mean drag coefficient $\overline{C}_D \approx 1.10$; *rms* lift coefficient $C'_{L,rms} \approx 0.52$; Strouhal number $St \approx 0.19$; and base pressure coefficient $-\overline{C}_{pb} \approx 1.25$ (presented in Figure 11).

The structured grids (S1-S3) show a consistent improvement as the grid is refined. $\overline{C}_D$, $C'_{L,rms}$ and $-\overline{C}_{pb}$ increase as the grid is refined, while St decreases. Hence further grid refinement may provide additional improvement in these integral parameters. Notice for S3 however that St reduces below the comparison value. This is an indication that sampling over more cycles or using a smaller time step should improve the results for this case; the non-zero value of the mean lift $\overline{C}_L$ supports this conclusion.

The unstructured grids show a slightly different trend. For the finest grid (U3), the mean drag and base pressure coefficient reduces compared to U2, which is the closest result to the experimental value. In addition, $C'_{L,rms}$ and St decrease from U2 to U3, despite all simulations showing good convergence and a mean lift of zero. This highlights the difficulty of performing grid refinement studies on unstructured grids. A more comprehensive assessment of the behaviour of results could be made through further grid refinement, which was outside of the scope of the current work.

Since it showed the best results and requiring that the moderate grid size be maintained, grid U2 was used for the investigations presented in Section 5.

5. Effect of Modelling on Flow Resolution

5.1. Turbulence model

A large difference in mean values is seen between the Smagorinsky (Case 5A) and dynamic mixed Smagorinsky models (Case 4E). The simpler Smagorinsky model significantly over-predicts $\overline{C}_D$; this is due to the fixed value of C_S, which adds too much dissipation. Dynamically adjusting C_S both in space and time improves the dissipation level provided by the subgrid model. A similar effect is observed for $C'_{L,rms}$ and $-\overline{C}_{pb}$. This result comes as no surprise, and agrees with the results of [10, 15]. Hence we used the dynamic Smagorinsky model for all other cases, and focussed on investigating the choice of convection differencing scheme.

5.2. Convection scheme

Since the grid resolution will the behaviour of the numerical schemes, we chose to investigate a number of options within OpenFOAM for interpolation of fluxes in the convective acceleration term. These were outlined in Section 5.

Time traces of lift and drag for cases using different numerical schemes are shown in Figure 5. Corresponding spectra were calculated as power spectral densities using Welch's [33] fast Fourier transform algorithm, and are shown in Figure 6. The lift spectrum, in dB, is defined as

$$\Phi_{LL}(\omega) = 10 \log_{10} \left[\int_{-\infty}^{\infty} r_L(\tau) e^{-i\omega\tau} d\tau \right], \qquad (12)$$

where τ is the time lag and $r_L = \overline{C_L(t) C_L(t+\tau)}$ is the autocorrelation of the lift coefficient.

Another measure indicative of the near-wake and boundary layer physics is the mean surface pressure coefficient $\overline{C}_p$, defined here as

$$\overline{C}_p = \frac{2\overline{p - p_0}}{\rho_0 U_0^2} \qquad (13)$$

where p_0, ρ_0 and U_0 are the reference pressure, density and velocity. This is plotted against θ, where $\theta = 0^\circ$ corresponds to the stagnation point (see Figure 1). $\overline{C}_p$ is shown in Figure 7, for the same cases as Figures 5 and 6.

Firstly we discuss the second-order schemes, QUICK and linear, referring to Figures 5(a), 6(a) and 7(a). The FL100 and QUICK schemes provide very similar results, both in terms of the fluctuating forces and mean surface pressure. This is in contrast to the linear scheme, which shows reduced fluctuations levels in addition to a lower mean drag. Figure 6(a) shows not only the reduced broadband level in the lift coefficient, but also the increased Strouhal number. In Figure 7(a), the shape of the $\overline{C}_p$ distribution is very different to the other schemes; this indicates a later mean separation point, while the lower value of $-\overline{C}_{pb}$ is attributed to a small recirculation length behind the cylinder. These results lead to the conclusion that the linear scheme has artificially increased the Reynolds number. This is clearly not desired, hence the schemes introducing upwinding are preferable in this case. Of these two, FL100 shows the best prediction of the integral parameters, although running QUICK for longer could improve these data, since $\overline{C}_L$ is non-zero.

Cases using different amounts of upwinding are now compared. Figure 5(b) shows that only adding 10% upwinding when using the FL scheme is not enough to overcome the issues associated with the linear scheme; the drag still much lower than FL100 and the fluctuations are smaller. Figure 6(b) shows that the over-prediction of the Strouhal number is not as large however, while $C'_{L,rms}$ also increases slightly. In addition, the surface pressure coefficient for FL10 is in closer agreement with FL100 on the front half of the cylinder. Using a fixed amount of upwinding (LL10) only gives a discrepancy with FL100 on

Table 3: Summary of all simulated cases. SGS is subgrid scale model, FL and LL are filteredLinear and limitedLinear convection schemes. Case numbering reflects the section of the paper in each the results are presented. For $Re = 6.31 \times 10^4$, cases 6B and 6C use different grids (denoted U2.1 and U2.2) where the domain width has been increased to πD and $2\pi D$ respectively, while maintaining the same number of cells; case 6F uses grid U3.

Case	$Re/10^5$	Grid	SGS	Conv.	% upwind	$\overline{C}_D$	$\overline{C}_L$	$C'_{L,rms}$	St	$-\overline{C}_{pb}$
4A	1.26	S1	DMS	FL	up to 100	0.85	-0.01	0.46	0.207	0.58
4B		S2				0.95	0.11	0.55	0.207	0.88
4C		S3				1.00	-0.25	0.63	0.177	1.01
4D		U1				0.81	-0.01	1.02	0.253	0.76
4E		U2				1.10	0.04	0.58	0.205	1.13
4F		U3				0.89	0.00	0.50	0.203	0.86
5A	1.26	U2	S	FL	100	1.56	0.04	1.06	0.189	1.67
5B			DMS	QUICK	12.5	1.05	-0.11	0.76	0.212	0.99
5C				linear	0	0.43	0.00	0.26	0.331	0.47
5D				FL	up to 10	0.58	0.00	0.32	0.285	0.59
5E				LL	10	0.79	-0.02	0.32	0.189	0.67
5F					100	0.88	0.00	0.47	0.189	0.77
6A	0.63	U2	DMS	FL	up to 100	1.43	0.02	1.00	0.201	1.64
6B		U2.1				1.33	0.02	0.76	0.189	1.42
6C		U2.2				1.27	0.01	0.63	0.189	1.36
6D	2.52	U2				0.42	0.00	0.25	0.284	0.45
6E	3.15					0.39	0.00	0.25	0.303	0.41
6F	5.06	U3				0.31	0.01	0.10	0.342	0.35

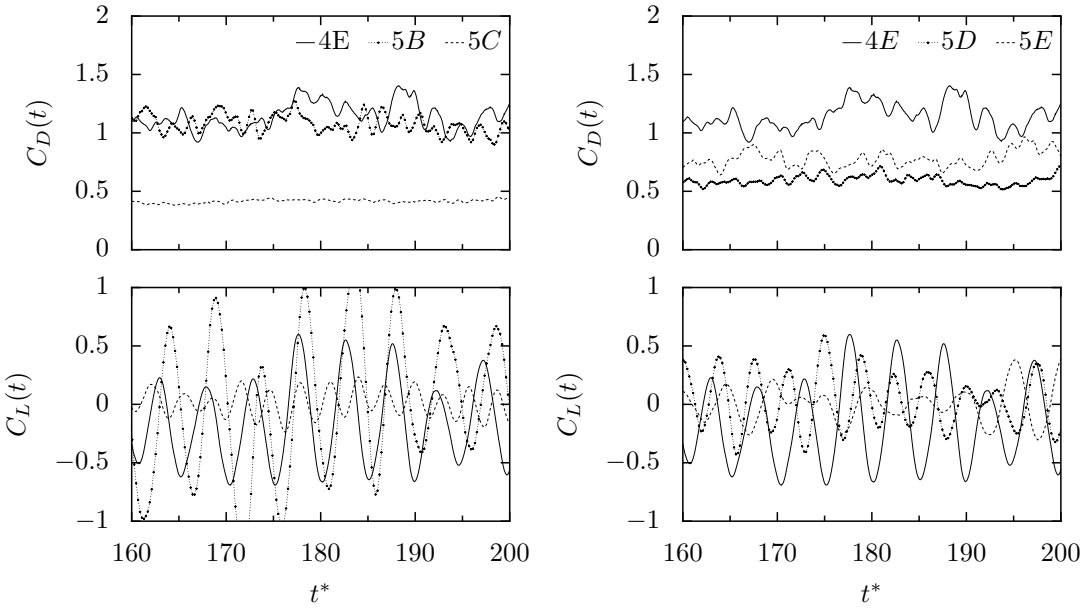

(a) FL100, QUICK and linear

(b) FL100, FL10 and LL10

Figure 5: Time traces of lift and drag coefficient for cases selected to highlight the influence of convection schemes. Time normalised as $t^* = tU_0/D$. Naming convention is scheme + percentage of upwinding.

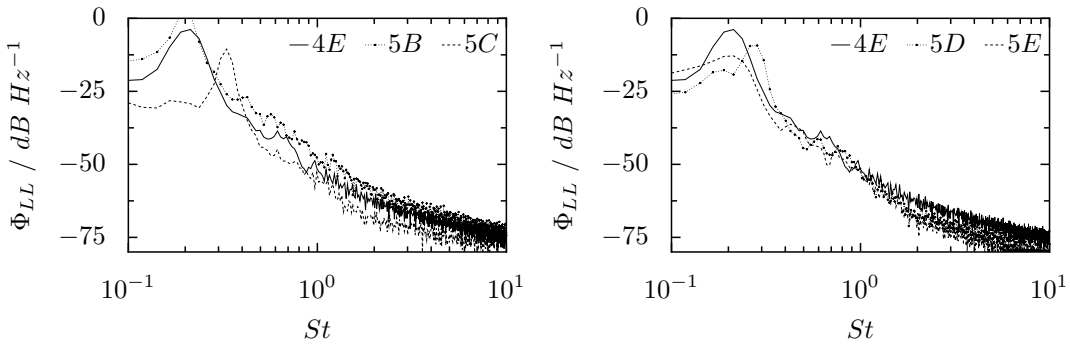

(a) FL100, QUICK and linear

(b) FL100, FL10 and LL10

Figure 6: Power spectral density of the lift coefficient for cases selected to highlight the influence of convection schemes.

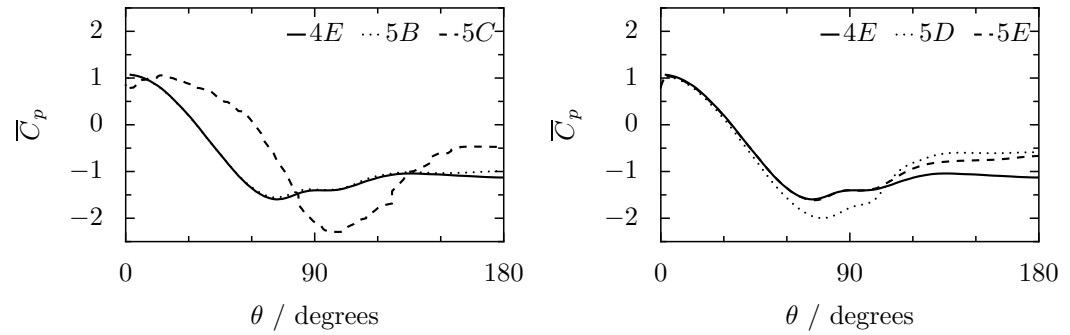

(a) FL100, QUICK and linear

(b) FL100, FL10 and LL10

Figure 7: Surface pressure coefficient for cases selected to highlight the influence of convection schemes.

the back half of the cylinder. Using this scheme, the mean drag increases somewhat towards the comparison value, as does the magnitude of the fluctuating forces (indicated by $C'_{L,rms}$

Figure 8 shows axial velocity slices for the six cases involving different convection schemes, providing an overview of the effect of the schemes on the resolved flow. In general the central schemes, as expected, resolve more fine scale turbulence compared to the upwind schemes. Despite this, linear (Figure 8(c)) and FL10 (Figure 8(d)) exhibit non-physical flow features, particularly close to the cylinder and at the grid refinement boundaries. The FL100 case, which adds upwinding dynamically, shows the best global resolution of turbulence. Although the QUICK scheme showed acceptable results in terms of the integral parameters, the fixed level of upwinding (which is similar to LL10) means that eddies are not as well resolved.

6. Predictions Over a Range of Reynolds Numbers

Finally, results of predictions for a range of Reynolds numbers surrounding the drag crisis are given. All the simulations used the FL100 convection scheme; grid U2 was initially used for all cases, although additional grids were required for two cases. Note therefore that the Δx^+, y_w^+ and Δz^+ values from Table 2 are different.

6.1. Overall results

The wake flow for four of the Reynolds numbers is visualised in Figure 9. The change in vortex dynamics with Reynolds number is clearly observed. At $Re = 6.31 \times 10^4$, large scale vortices are seen, with long streamwise structures and less fine scale turbulence. Kelvin-Helmholtz vortices are also evident in the shear layer. As the Reynolds number increases, the wake turbulence becomes increasingly broadband, with faster breakdown of the shear layer, and later separation of the boundary layer. This behaviour was described in Section 1.

The transition from coherent to broadband wake turbulence as Reynolds number increases is seen in the magnitude of the lift fluctuations presented in Figure 10(a). The lower spectral amplitude in Figure 10(b) for Case 6D also shows this, while the larger secondary peak in the spectrum for Case 6A indicates the stronger shear layer for this lower Reynolds number.

The surface pressure coefficient for all four Reynolds numbers is displayed in Figure 10(c). This value has previously been used as an indicator of the near-wake flow regime. The shift in minimum surface pressure to higher θ as Reynolds number increases reveals the latter separation of the boundary layer. Associated with this is a reduction in $\overline{C}_{pb}$. This behaviour is expected from the experimental data collated by Williamson [3]. High $\overline{C}_{pb}$ indicates a large separated region behind the cylinder, as is seen for lower

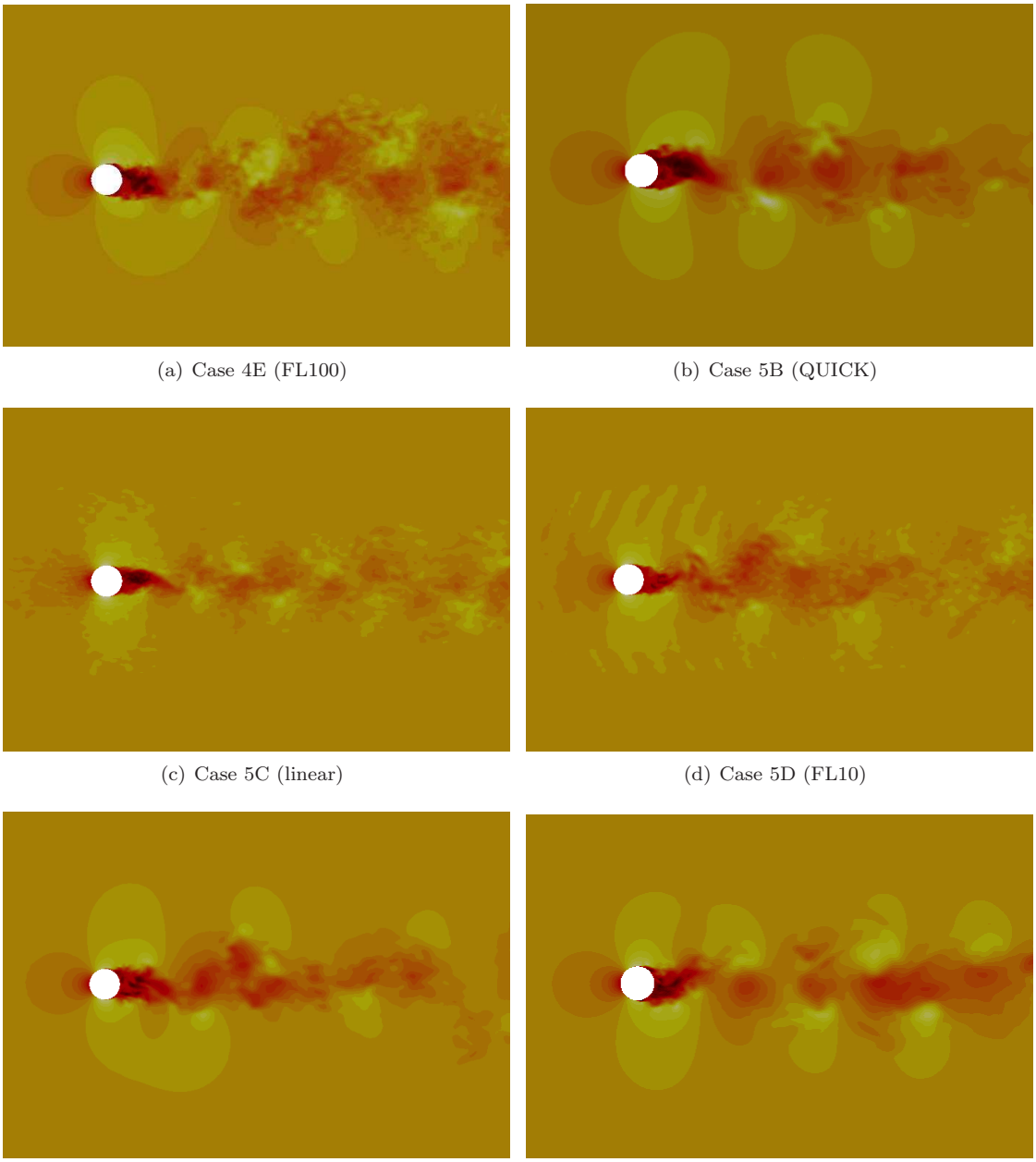

(a) Case 4E (FL100)

(b) Case 5B (QUICK)

(c) Case 5C (linear)

(d) Case 5D (FL10)

(e) Case 5E (LL10)

(f) Case 5F (LL100)

Figure 8: Normalised axial velocity slices at domain centreline: u/U_0. Values from -1.15 (dark) to 1.85 (light).

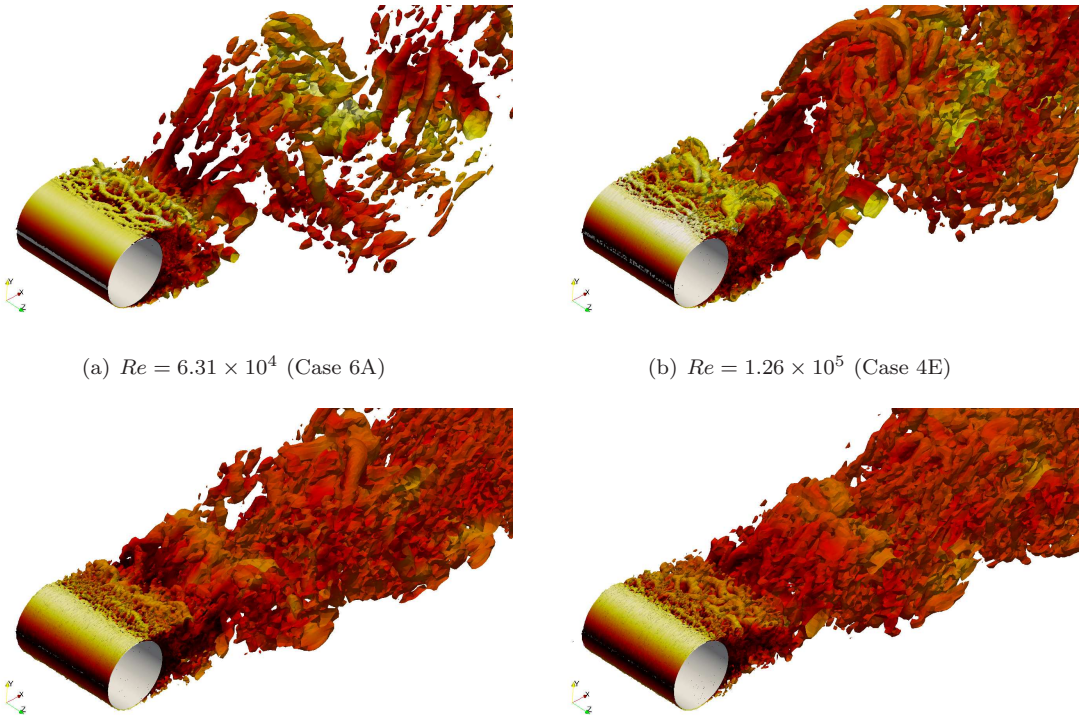

(a) $Re = 6.31 \times 10^4$ (Case 6A)

(b) $Re = 1.26 \times 10^5$ (Case 4E)

(c) $Re = 2.52 \times 10^5$ (Case 6D)

(d) $Re = 3.15 \times 10^5$ (Case 6E)

Figure 9: Isosurfaces of $Q = 10\ s^{-1}$, coloured by streamwise velocity, for range of Reynolds numbers.

Reynolds numbers.

Mean drag, *rms* lift, Strouhal number and base pressure coefficient are compared to experimental and empirical estimates provided by [3, 4, 5, 34] in Figure 11. Depending on which experimental data set is used, the Re at which the drag crisis occurs changes. It appears that the LES predicts an earlier drag crisis, more similar to the data 'other exp' than the 'MARIN exp' of [1] and [34]. However, since $Re = 2.52 \times 10^5$ lies in the 'upper critical' flow regime, this case is more difficult to simulate, due to asymmetry of the boundary layer transition and separation. This should lead to a non-zero value of the mean lift (not seen here). Hence a finer grid should be used for this case. For example, the drag and Strouhal number are better predicted when using 90 million tetrahedral cells [14].

When this is considered alongside the empirical fit of $C'_{L,rms}$ and $-\overline{C}_{pb}$, the large reduction in fluctuating lift occurs too early. The Strouhal number is also seen to increase by $\sim 50\%$ after the drag crisis. This is more than expected, but displays the correct trend. After the drag crisis, the flow becomes easier to simulate, and the predictions are favourable at $Re = 5.06 \times 10^5$. Note however that the finest grid (U3) was used here since U2 was divergent.

6.2. Effect of domain width at $Re = 6.31 \times 10^4$

Another consideration when assessing the suitability of the grids used is the domain width. This effect is most pronounced for lower Reynolds numbers, where the spanwise correlation length (Λ) increases (see *e.g.* Norberg [4]). The domain width of $1.7D$ is of a size typically used for simulations at high Reynolds numbers, yet it provides poor predictions for $Re = 6.31 \times 10^4$.

At this Reynolds number, the flow exhibits quite a different behaviour in terms of the increased size of the shed vortices. Thus the location of the simulation boundaries has more impact on the flow; since periodic boundary conditions are used, Λ may become infinite.

For this Reynolds number, Norberg [4] estimates $\Lambda/D \approx \pi$. Therefore two additional grids were created to investigate the effect of spanwise domain width on the results; U2.1 as width πD, and U2.2 has $2\pi D$. In both cases the existing grid U2 was stretched without changing the total number of cells, hence reducing the spanwise resolution in each case.

From Table 3 and Figure 11, it can be seen that the increased domain width has a large effect on the results. The widest domain, where $\Lambda/D \approx 2$ shows the closest results to the comparison data for all parameters. The largest effect is seen on the fluctuating lift, since this measure is related to the circulation, which is artificially increased by the narrower domains. Hence we conclude that domain width, rather than spanwise resolution, is more important at this Reynolds number.

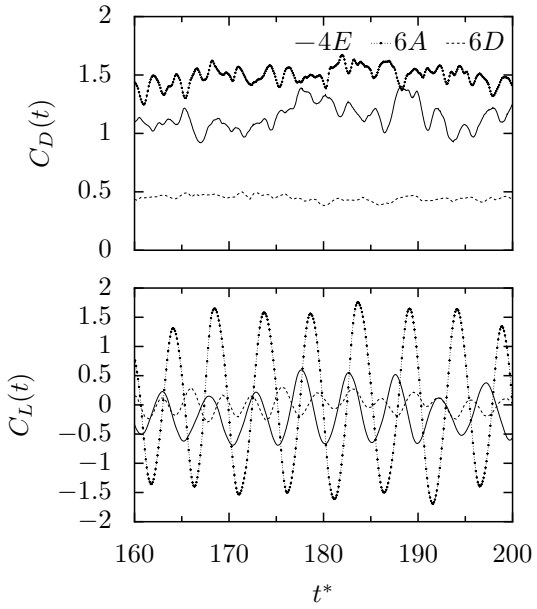

(a) Time traces of the lift and drag coefficients

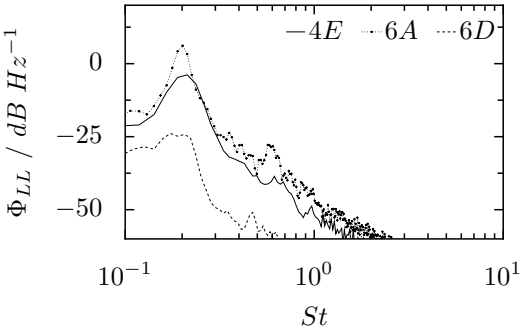

(b) Power spectral density of the lift coefficient

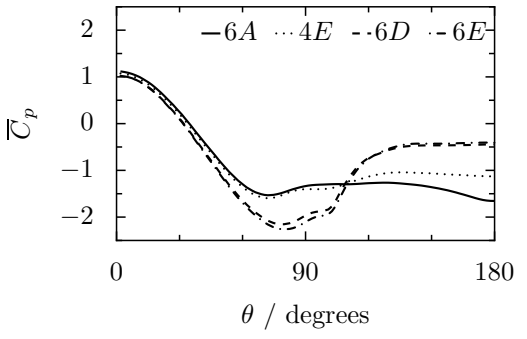

(c) Surface pressure coefficient

Figure 10: Force oefficient and surface pressure results for different Reynolds numbers.

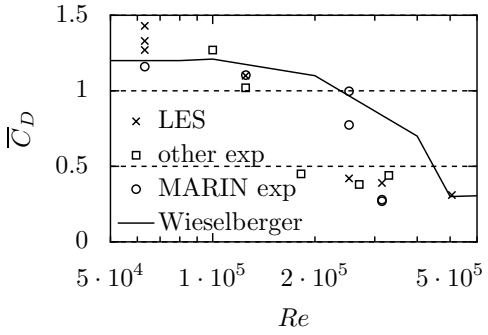

(a) Drag coefficient. Comparison experimental data from Rosetti *et al.*[5]; 'Wieselberger' data taken from [34].

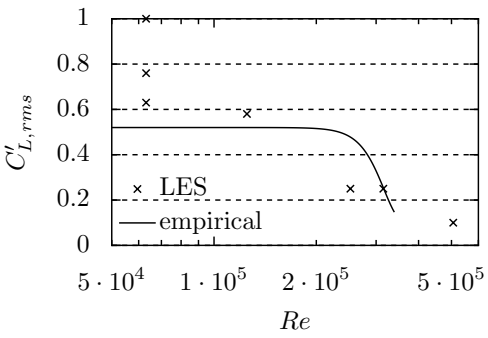

(b) *rms* lift coefficient. Comparison is empirical formulation taken from Norberg, Appendix A. [4].

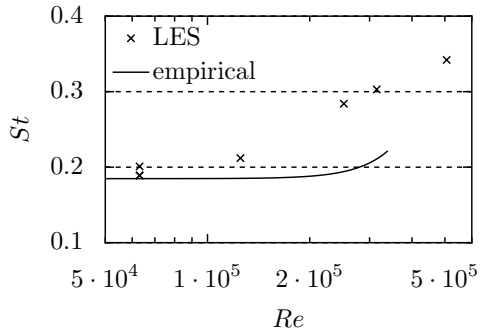

(c) Strouhal number. Comparison is empirical formulation taken from Norberg, Appendix A. [4].

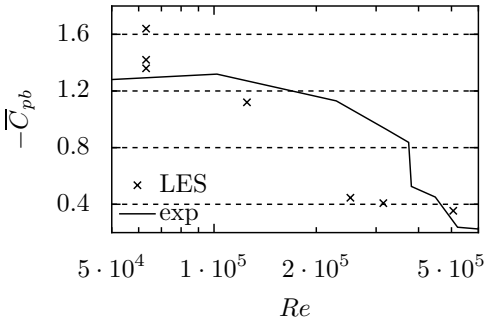

(d) Base pressure coefficient. Comparison experimental data from Williamson [3].

Figure 11: Integral parameters for the five Reynolds numbers simulated. For the $Re = 6.31 \times 10^4$ case, the results show better agreement with the experimental/empirical data as the domain width is increased.

7. Discussion and Conclusions

This work is one of only a few LES studies of circular cylinders at high Reynolds numbers. Whilst the results are encouraging, they should be treated with caution. This is due to the high interdependence between Reynolds number, grid size, grid refinement and turbulence modelling. The path to the preferred numerical settings was evidently not linear. We have identified which aspects of the modelling appear to have the largest effect on the flow resolution and integral measures. The aim was not to provide 'optimal' settings; as mentioned these are problem specific, and potentially also code specific. Thus further verification and validation are required.

Our preference for the unstructured gridding strategy is not only the ability to focus the refinement more effectively. Using *snappyHexMesh*, square cells may be used throughout the domain, making the grid better designed for isotropic eddy-viscosity turbulence models. The sudden change in cell size across refinement region boundaries is however an issue, and these should be placed away from key flow features. In general, the characteristic flow features for the range of Reynolds numbers simulated were well captured, including separation point and transition via Kelvin-Helmholtz instability modes. Although only one grid was used for all Reynolds numbers, it is expected the improvements in the results could be obtained by more localised refinement. For example, at $Re = 6.31 \times 10^4$, streamwise refinement of the shear layer region could capture transition more accurately. Sizing refinement regions *a priori* is however not easy, and there is potential for further improvement through re-meshing *a posteriori* or adaptive grid refinement techniques.

Addressing high fidelity flow modelling (LES) on relatively coarse grids is important for engineering problems, and should be treated more frequently as computing resources increase further. Simulations presented here typically required 5×10^3 CPU hours, which is not unreasonable for benchmark studies such as this. When coarse grids are used in LES, the effect of numerical modelling on flow resolution is increased. In particular, we found that the more 'conventional' convection scheme (linear) does not provide good results, and actually seems to artificially increase the Reynolds number. The OpenFOAM convection scheme filteredLinear was found to be preferable, since an amount of upwinding is added dynamically. This avoids non-physical wiggles in the solution caused by the fully central scheme, whilst also removing unnecessarily high numerical dissipation introduced by the limitedLinear scheme.

The results presented here represent a fraction of the data obtained from the reported cases. As well as lift spectra and surface pressure, many more measures could be extracted, and compared to experiments. These could include: wake velocity and Reynolds stress profiles; wake velocity spectra; subgrid viscosity contribution from turbulence models; and frictional and pressure drag components. Since the present results were obtained as part of the International Towing Tank Conference Workshop on Wave Run-up and Vortex Shedding, the Reynolds numbers simulated do not correspond with commonly used test cases. Further validation of the numerical schemes investigated here could be made at $Re = 1.4 \times 10^5$ by comparing to [35].

Acknowledgements

This work was carried out as part of the International Towing Tank Conference Workshop on Wave Run-up and Vortex Shedding, held in Nantes, France during October 2013. We thank the other participants for their useful comments received during the workshop. Computations were performed using the Iridis 4 HPC cluster at the University of Southampton. Thanks to Gabriel Weymouth, Björn Windén (University of Southampton) and Henry Bandringa (University of Groningen/MARIN) for useful discussions regarding the numerical schemes.

References

[1] de Wilde JJ, Huijsmans RHM, Tukker J. Experimental investigation into the vortex formation in the wake of an oscillating cylinder using Particle Image Velocimetry. ISOPE 2006;:1–10.

[2] Feymark A, Alin N, Bensow R, Fureby C. Numerical simulation of an oscillating cylinder using large eddy simulation and implicit large eddy simulation. Journal of Fluids Engineering 2012;134(3):031205–1 – 031205–10. doi:\bibinfo{doi}{10.1115/1.4005766}.

[3] Williamson CHK, Williamson . Vortex dynamics in the cylinder wake. Annual Review of Fluid Mechanics 1996;28(1):477–539. doi:\bibinfo{doi}{10.1146/annurev.fl.28.010196.002401}.

[4] Norberg C. Fluctuating lift on a circular cylinder: review and new measurements. Journal of Fluids and Structures 2003;17(1):57–96. doi:\bibinfo{doi}{10.1016/S0889-9746(02)00099-3}.

[5] Rosetti GF, Vaz G, Fujarra ALC. URANS calculations for smooth circular cylinderflow in a wide range of Reynolds numbers: solution verification and validation. Journal of Fluids Engineering 2012;134(12):121103–1. doi:\bibinfo{doi}{10.1115/1.4007571}.

[6] Vaz G, Mabilat C, van der Wal R, Gallagher P. Viscous flow computations on smooth cylinders, a detailed numerical study with validation. In: Proceedings of the 26th International Conference on Offshore Mechanics and Arctic Engineering. 10th-15th June, San Diego; 2007,.

[7] Travin A, Shur M, Strelets M. Detached-Eddy Simulations Past a Circular Cylinder 2000;:293–313.

[8] Lysenko DA, Ertesvå g IS, Rian KE. Modeling of turbulent separated flows using OpenFOAM. Computers and Fluids 2013;80:408–22. doi:\bibinfo{doi}{10.1016/j.compfluid.2012.01.015}.

[9] Lysenko DA, Ertesvå g IS, Rian KE. Large-eddy simulation of the flow over a circular cylinder at Reynolds number 3900 using the OpenFOAM toolbox. Flow, Turbulence and Combustion 2012;89(4):491–518. doi:\bibinfo{doi}{10.1007/s10494-012-9405-0}.

[10] Breuer M. Numerical and modeling influences on large eddy simulations for the flow past a circular cylinder. International Journal of Heat and Fluid Flow 1998;19:512–21. doi:\bibinfo{doi}{10.1016/S0142-727X(98)10015-2}.

[11] Bandringa HJ, Verstappen RWCP, Wubs FW, Klaij CM, van der Ploeg A. Towards large-eddy simulation of complex

flows in maritime applications. In: Onate E, Oliver J, Huerta A, editors. Proceedings of the 6th European Conference on Computational Fluid Dynamics. Barcelona; 2014, p. 4700–11.
[12] Lehmkuhl O, Borrell R, Rodríguez I, Pérez-Segarra C, Oliva A. Assessment of the symmetry-preserving regularization model on complex flows using unstructured grids. Computers & Fluids 2012;60:108–16. doi:\bibinfo{doi}{10.1016/j.compfluid.2012.02.030}.
[13] Rodríguez I, Lehmkuhl O, Borrell R, Paniagua L, Pérez-Segarra CD. High performance computing of the flow past a circular cylinder at critical and supercritical Reynolds numbers. Procedia Engineering 2013;61:166–72. doi:\bibinfo{doi}{10.1016/j.proeng.2013.07.110}.
[14] Rodríguez I, Lehmkuhl O, Chiva J, Borrell R, Oliva A. On the wake transition in the flow past a circular cylinder at critical Reynolds numbers. In: Onate E, Oliver J, Huerta A, editors. Proceedings of 6th European Conference on Computational Fluid Dynamics. Wccm Xi; Barcelona; 2014, p. 5520–7.
[15] Breuer M. A challenging test case for large eddy simulation: high Reynolds number circular cylinder flow. International Journal of Heat and Fluid Flow 2000;21(5):648–54. doi:\bibinfo{doi}{10.1016/S0142-727X(00)00056-4}.
[16] Weller HG, Tabor GR, Jasak H, Fureby C. A tensorial approach to computational continuum mechanics using object-oriented techniques. Computers in Physics 1998;12(6):620–31. doi:\bibinfo{doi}{10.1063/1.168744}.
[17] Jasak H, Jemcov A, Tuković v. OpenFOAM: A C++ library for complex physics simulations. In: International Workshop on Coupled Methods in Numerical Dynamics. 19th-21st September, Dubrovnik; 2007, p. 47–66.
[18] Rhie C, Chow W. Numerical study of the turbulent flow past an airfoil with trailing edge separation. AIAA Journal 1983;21:1525–32. doi:\bibinfo{doi}{10.2514/3.8284}.
[19] Issa RI. Solution of the implicitly discretised fluid flow equations by operator-splitting. Journal of Computational Physics 1986;62(1):40–65. doi:\bibinfo{doi}{10.1016/0021-9991(86)90099-9}.
[20] Pope SB. Turbulent flows. Cambridge: Cambridge University Press; 2000. ISBN 978-0521598866.
[21] Sagaut P. Large eddy simulation for incompressible flows. Berlin: Springer-Verlag; 2006. ISBN 978-3540263449.
[22] Georgiadis NJ, Rizzetta DP, Fureby C. Large-eddy simulation: Current capabilities, recommended practices, and future research. AIAA Journal 2010;48(8):1772–84. doi:\bibinfo{doi}{10.2514/1.J050232}.
[23] Smagorinsky J. General circulation experiments with the primitive equations. I. The basic experiment. Monthly Weather Review 1963;91(3):99–165. doi:\bibinfo{doi}{10.1175/1520-0493(1963)091⟨0099:GCEWTP⟩2.3.CO;2}.
[24] Bardina J, Ferziger JH, Reynolds WC. Improved subgrid-scale models for large eddy simulation. In: AIAA Fluid and Plasma Dynamics Conference. 14th-16th July, Snowmass; 1980,doi:\bibinfo{doi}{10.2514/6.1980-1357}.
[25] Germano M, Piomelli U, Moin P, Cabot W. A dynamic subgrid-scale eddy viscosity model. Physics of Fluids 1991;3(7):1760–5. doi:\bibinfo{doi}{10.1063/1.857955}.
[26] Lilly DK. A proposed modification of the Germano subgrid-scale closure method. Physics of Fluids 1992;4(3):633–5. doi:\bibinfo{doi}{10.1063/1.858280}.
[27] Zang Y, Street R, Koseff J. A dynamic mixed subgrid-scale model and its application to turbulent recirculating flows. Physics of Fluids A: Fluid Dynamics 1993;5(12):3186–96. doi:\bibinfo{doi}{10.1063/1.858675}.
[28] Filip GP, Maki KJ, Kim Se. Critical Evaluation of Several LES and DES Models for Simulation of Flow Around a Vertical Surface-Piercing Cylinder 2012;(October).
[29] Lloyd TP. Large eddy simulations of inflow turbulence noise: application to tidal turbines. Ph.{D}. thesis; University of Southampton; 2013.
[30] Versteeg HK, Malalasekera W. An introduction to fluid dynamics: The finite volume method. Harlow: Longman Group; 1995. ISBN 0-582-21884-5.
[31] Sweby PK. High resolution schemes using flux limiters for hyperbolic conservation laws. SIAM Journal on Numerical Analysis 1984;21(5):995–1011. doi:\bibinfo{doi}{10.1137/0721062}.
[32] Leonard BP. A stable and accurate convective modelling procedure based on quadratic upstream interpolation. Computer Methods in Applied Mechanics and Engineering 1979;19:59–98. doi:\bibinfo{doi}{10.1016/0045-7825(79)90034-3}.
[33] Welch P. The use of fast Fourier transform for the estimation of power spectra. IEEE Transactions on Audio Electroacoustics 1967;15(2):70–3. doi:\bibinfo{doi}{10.1109/TAU.1967.1161901}.
[34] Schlichting H. Boundary layer theory. New York: McGraw-Hill; 7th ed.; 1979.
[35] Cantwell B, Coles D. An experimental study of entrainment and transport in the turbulent near wake of a circular cylinder. Journal of Fluid Mechanics 1983;136:321–74. doi:\bibinfo{doi}{10.1017/S0022112083002189}.